Nuclear Materials and Energy 19 (2019) 479–486

Contents lists available at ScienceDirect

Nuclear Materials and Energy

journal homepage: www.elsevier.com/locate/nme

Inter-ELM pedestal localized fluctuations in tokamaks: Summary of multi-machine observations

F.M. Laggner*[a,b], A. Diallo[b], M. Cavedon[c], E. Kolemen[a]

[a] Princeton University, Princeton, New Jersey 08544, United States of America
[b] Princeton Plasma Physics Laboratory, Princeton, New Jersey 08543, United States of America
[c] Max Planck Institute for Plasma Physics, Boltzmannstr. 2, Garching, 85748 Germany

ARTICLE INFO

Keywords:
Plasma
High confinement mode (H-mode)
Edge localized mode (ELM)
Pedestal profiles
Edge instabilities

ABSTRACT

A variety of experimental studies on pedestal localized fluctuations appearing in between crashes of edge localized modes (ELMs) across several tokamaks have been reviewed and summarized. The onset of the inter-ELM fluctuations is correlated with the evolution of the pedestal gradients. Three profile recovery phases are extracted, which are interlinked with the onsets of different kinds of pedestal fluctuations. Across machines it is found that the pedestal fluctuations can be assorted into at least three categories. These are determined by the fluctuation onset in the ELM cycle, observed frequency range and radial location in the pedestal. Further, the categories might be also related to different instabilities. Similar observations at various machines may point to a underlying generation mechanism that acts similarly for presently accessible pedestal parameter ranges.

1. Introduction and motivation

More than 35 years after its initial discovery, the high confinement mode (H-mode) [1] has been achieved and studied in a large number of magnetic confinement fusion experiments [2,3]. H-mode is the designated operation scenario for ITER [4], because of its improved plasma confinement. Its origin lies in the establishment of an edge transport barrier (ETB), which leads to a steep pressure gradient at the plasma edge, forming the pedestal. The overall plasma performance in H-mode strongly depends on the pedestal pressure. In general, the pedestal is globally limited by edge localized modes (ELMs) [5,6], which periodically relax the ETB. This leads to a collapse of the pedestal and expulsion of heat and particles towards the wall. In ITER large ELMs will exceed material limits [7,8], making ELM control or avoidance a necessity [9–11].

The leading explanation for the instabilities underlying the ELM-related pedestal limit is the destabilization of coupled peeling-ballooning (PB) modes [12], which critically grow above a certain normalized pressure gradient (α) and average toroidal current density in the pedestal ($\langle j_{tor} \rangle$). However, this model does not provide any information on the achievable pedestal pressure and, therefore, the resulting plasma performance. In order to predict and optimize future fusion devices, deep understanding of the plasma edge and its behavior is required. Microinstabilities are expected to play a major role in regulating the profile gradients at a sub-critical level with marginal stability for PB modes [13–19]. Nevertheless, from an experimental point of view it is not fully understood, which mechanisms determine the pedestal structure. Over the last few years, a variety of publications identified and studied instabilities that are present in the pedestal in between ELMs. These are mostly detected by fluctuation diagnostics and might play a key role in determining the pedestal structure. Additional support is given by studies, which link the pedestal profile dynamics with pedestal fluctuation measurements. Further, similar to the occurrence of H-mode and ELMs, these pedestal fluctuations have been identified and studied in various tokamaks, suggesting an universal underlying generation mechanism.

The aim of this paper is to summarize and review the large number of experimental studies on pedestal fluctuations in between type-I ELMs, which are the largest kind of ELMs in terms of their energy loss. The common observations from several tokamaks are condensed into an abstract picture of the pedestal dynamics and associated onsets of inter-ELM pedestal instabilities. A brief introduction to main quantities that drive or damp pedestal instabilities is provided in Section 2. The inter-ELM pedestal profile evolution and its interlink to the onset of pedestal fluctuations is outlined in Section 3. Section 4 presents a review of work on inter-ELM pedestal fluctuations across several tokamaks. The observed instability structure is discussed in Section 5. Section 6 contains an outlook towards addressing open questions.

* corresponding author.
E-mail addresses: flaggner@princeton.edu (F.M. Laggner), ekolemen@princeton.edu (E. Kolemen).

https://doi.org/10.1016/j.nme.2019.02.030
Received 1 August 2018; Received in revised form 4 February 2019; Accepted 21 February 2019
Available online 10 April 2019

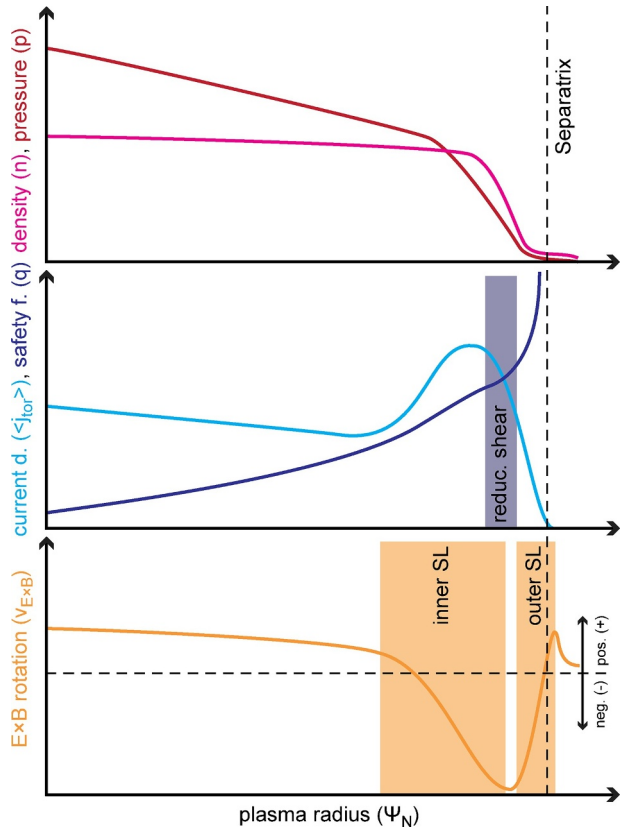

Fig. 1. Plasma edge profiles: (top) density (n) and thermal pressure (p), (center) average toroidal current density in the pedestal ($\langle j_{\mathrm{tor}} \rangle$) and safety factor ($q$) and (bottom) E × B rotation velocity ($\nu_{\mathrm{E\times B}}$). While a steep thermal pressure gradient (∇p) and a high $\langle j_{\mathrm{tor}} \rangle$ drive instabilities, sheared flow velocities (inner and outer shear layer (SL)) tear them apart and reduce them.

2. Drive and damping mechanisms of pedestal instabilities

Magnetohydrodynamic (MHD) instabilities are driven by current or pressure gradient. ELMs, respectively PB modes, are MHD instabilities, which are destabilized in the region of the ETB. Here, steep pressure gradients are present, which themselves drive the bootstrap current, leading to high total toroidal currents and an interlink of pressure gradient and current. Moreover, the bootstrap current (j_{BS}) has dependencies on several plasma parameters of which the practically most relevant ones are listed:

$$j_{\mathrm{BS}} = f(\nabla p,\ \nu^*,\ \epsilon,\ B_\theta), \tag{1}$$

using thermal pressure gradient (∇p), plasma collisionality (ν^*), inverse aspect ratio (ϵ) and poloidal magnetic field (B_θ). The individual profile gradients contribute with different proportionality coefficients to j_{BS}. The proportionality coefficients were approximated to be 0.5 for ∇n, 0.15 for ∇T_{e} and 0.1 for ∇T_{i} [20], which becomes important when the pedestal density and temperature profiles of electrons and ions evolve on separate timescales as discussed in Section 3.

Fig. 1 illustrates the plasma edge profiles that are of general importance, when discussing plasma edge instabilities. The top plot shows the (p) profile, as well as its contribution from the density (n). There is some degree of freedom, since contributions of ions and electrons as well as density and temperature determine the profile structure. Especially the location of the $\max(-\nabla p)$ with respect to the flux surfaces is not fixed due to the variable separatrix density, which can also impact the edge stability [21,22]. The edge current is mainly localized in the region of $\max(-\nabla p)$ (Fig. 1, middle plot). Because of the x-point topology there are local areas of reduced magnetic shear and the flux surface averaged (q) profile is flattened out. Therefore, this region is also prone to instabilities. Further, global plasma parameters like ratio of thermal to magnetic pressure (β) or edge rotation can affect the edge PB stability [23].

Steep profile gradients are also the underlying drive for a variety of microinstabilities [24], which can develop into turbulence and therefore strongly impacting transport. In contrast, the paradigm of the ETB is that turbulence is strongly suppressed by sheared plasma flows [25]. These are mainly due to the E × B rotation velocity ($\nu_{\mathrm{E\times B}}$) caused by the radial electric field (E_{r}). E_{r} can be determined from the radial force balance (see Eq. (2)) and it has been found that the diamagnetic term is dominant in the ETB region [26]:

$$E_{\mathrm{r}} = \frac{\nabla p_\alpha}{Z_\alpha e n_\alpha} - \nu_{\theta,\alpha} B_\phi + \nu_{\phi,\alpha} B_\theta, \tag{2}$$

using the species α with its corresponding pressure gradient (∇p_α) and charge (Z_α), the elementary charge (e), its density (n_α) as well as its poloidal rotation ($\nu_{\theta,\alpha}$) and its toroidal rotation ($\nu_{\phi,\alpha}$) and the toroidal magnetic field (B_ϕ). A typical $\nu_{\mathrm{E\times B}}$ profile is illustrated in the bottom plot of Fig. 1. On each side of its characteristic minimum, which is governed by the depth of the radial electric field well ($\max(-E_r)$), a shear layer (SL) is present. These are expected to suppress the edge turbulence and therefore, form the ETB. There are experimental findings, that though an ETB is present, residual inter-ELM heat transport occurs across the pedestal [27,28]. The ion heat transport in the steep gradient region is around the neoclassical estimate [29] but the electron heat conductivity can exceed this level [30]. Furthermore, inter-ELM pedestal fluctuations are another indication that there are instabilities present in the pedestal. Nevertheless, because of the sheared flow, the radial extent of the instability is thought to be either rather small, or the instability's location has to be such that its drive, the magnetic topology and the flow profile align, i.e. around the $\max(-E_{\mathrm{r}})$ where the velocity shear is lower.

3. Inter-ELM profile evolution

A variety of work investigated the pedestal profile dynamics in several tokamaks. There are studies from JET [31,32], MAST [33–35] and TCV [36] available, mainly focusing on the evolution of the pedestal top quantities, pedestal height and width. On ASDEX Upgrade (AUG) and DIII-D, it was found that the maximum electron density gradient ($\max(-\nabla n_{\mathrm{e}})$) is established before the maximum electron temperature gradient ($\max(-\nabla T_{\mathrm{e}})$) and that the maximum electron pressure gradient ($\max(-\nabla p_{\mathrm{e}})$) is clamped several milliseconds before the following ELM onset [37,38]. This has been also reported for a shaping variation in triangularity (δ) [39]. Further, the ion temperature (T_{i}) evolution has been studied at these two tokamaks [40–42]. Fig. 2 presents the pedestal profile gradient evolution of an AUG case. The recovery of the maximum ion temperature gradient ($\max(-\nabla T_{\mathrm{i}})$) occurs on similar timescales as $\max(-\nabla n_{\mathrm{e}})$, i.e. faster than $\max(-\nabla T_{\mathrm{e}})$. Furthermore, three characteristic phases of the inter-ELM profile recovery can be extracted:

Phase I: $\max(-\nabla n_{\mathrm{e}})$ and $\max(-\nabla T_{\mathrm{i}})$ recovery
Phase II: $\max(-\nabla T_{\mathrm{e}})$ recovery
Phase III: $\max(-\nabla p)$ clamping

A rough sketch of these phases is illustrated in Fig. 3, where the dark red line illustrates the evolution of $\max(-\nabla p)$ and the magenta line indicates the maximum density gradient ($\max(-\nabla n)$) recovery. As discussed in Section 2, j_{BS} is driven by the profile gradients. For this reason, the evolution of j_{BS}, or more generally $\langle j_{\mathrm{tor}} \rangle$, is interlinked with the profile evolution. This is illustrated in Fig. 3 by the cyan line, which indicates the evolution of the maximum average toroidal current density in the pedestal ($\max(\langle j_{\mathrm{tor}} \rangle)$). Further, detailed experimental studies investigated this inter-ELM evolution of the edge current

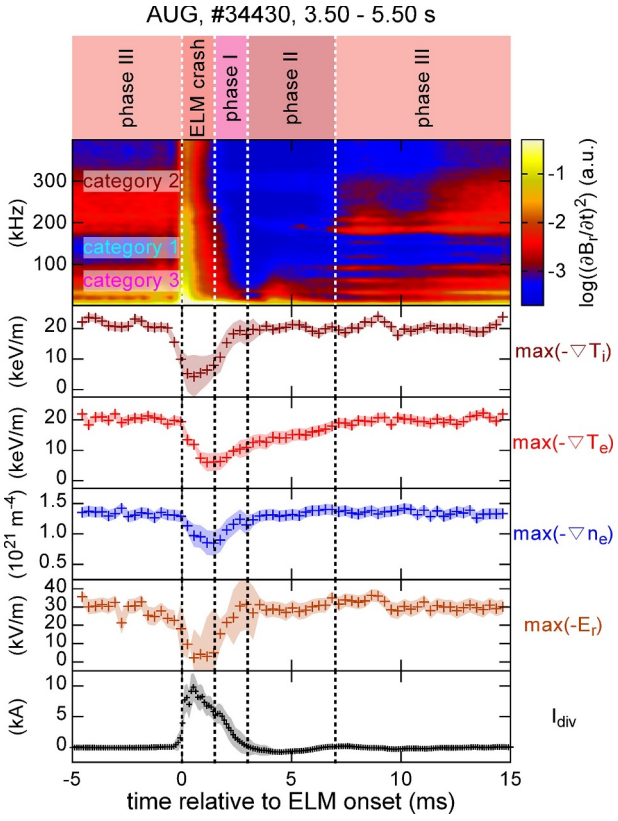

Fig. 2. Inter-ELM profile evolution and fluctuations: Spectrogram of radial magnetic field fluctuations ($\partial B_r/\partial t$), maximum ion temperature gradient ($\max(-\nabla T_i)$), maximum electron temperature gradient ($\max(-\nabla T_e)$), maximum electron density gradient ($\max(-\nabla n_e)$), depth of the radial electric field well ($\max(-E_r)$) and divertor shunt current (I_{div}). The pedestal profile recovery can be structured in three general phases, which all are accompanied by characteristic fluctuations. Figure reproduced from [43].

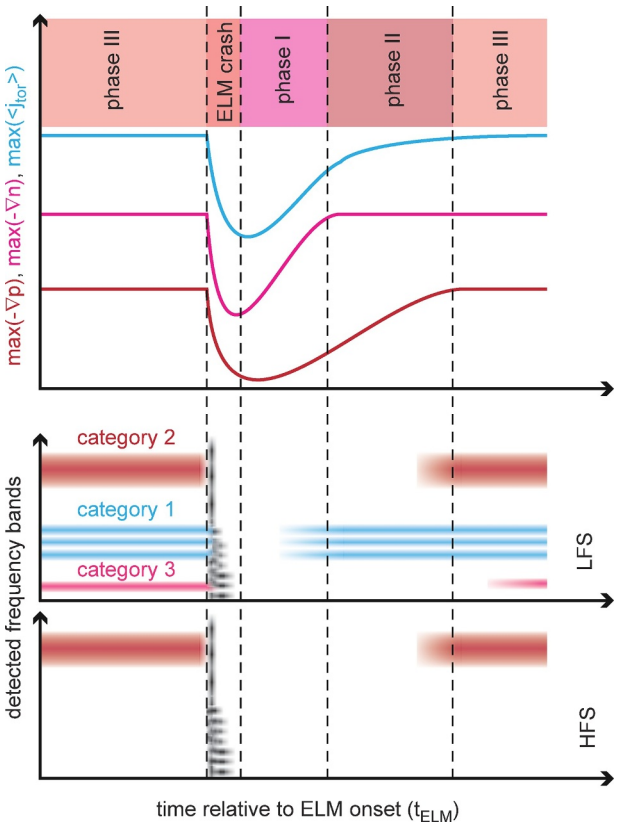

Fig. 3. Abstract view on the inter-ELM profile evolution and fluctuations: maximum average toroidal current density in the pedestal ($\max(\langle j_{tor}\rangle)$), maximum density gradient ($\max(-\nabla n)$), maximum thermal pressure gradient ($\max(-\nabla p)$) and illustrated fluctuation band structure. The pedestal profile recovery can be structured in three phases, which all are accompanied by characteristic fluctuations.

[44,45].

In AUG and DIII-D the profile gradient saturation is linked to the onset of pedestal localized fluctuations [46–48]. Similar fluctuations have also been observed in several machines and they are categorized in Section 4. During phase I of the profile recovery, typically very low fluctuation amplitudes are found over a wide spectral range [49] (see Fig. 2). The medium and higher frequency fluctuations with corresponding low and high toroidal mode number (n), which set in during phase II and phase III of the profile recovery have different low field side (LFS)-high field side (HFS) parity. This is indicated at the bottom of Fig. 3 and is an important feature when categorizing the kind of fluctuations. Further, the fluctuations occurring in phase II of the profile recovery typically have a band-like structure, whereas the fluctuations with onset in phase III appear to have a more broadband structure in the frequency domain. Therefore, it is likely that the underlying mode structure is a superposition of multiple mode numbers.

4. Overview on experimental observations

In the following, the main findings of several tokamaks on pedestal instabilities occurring in between type-I ELMs are summarized and categorized by similarities. Historically, it has been quite challenging to investigate these high frequency fluctuations, since digitizers with sampling rates in the region of 1MHz were not routinely available. Nevertheless, the first reports of high frequency events (on the order of several hundreds of kilohertz) date back to the early nineties. These have been mostly observed by their magnetic signature detected with Mirnov Coils (MCs). MCs are used to measure global fluctuations of the magnetic field, mostly in the radial or poloidal direction. Furthermore, toroidal and poloidal arrays of MCs can be utilized to determine the structure, i.e. n and poloidal mode number (m), of an instability. Also further developed fluctuation diagnostics as electron cylotron emission (ECE), providing profiles of T_e fluctuations, o-mode microwave reflectometry (RFL), measuring electron density (n_e) fluctuations at the cutoff density layer, beam emission spectroscopy (BES), performing 2-D imaging of n_e fluctuations, laser interferometry (LI), detecting line integrated n_e fluctuations, as well as lately electron cyclotron emission imaging (ECEI), measuring a 2-D image of the T_e fluctuations and cross polarization-Doppler backscattering (CP-DBS), accessing internal magnetic and n_e fluctuations, have been deployed to characterize the behavior of the inter-ELM pedestal fluctuations.

Table 1 summarizes the related work from several tokamaks in alphabetical order of their names and chronological order with respect to publication date within one machine. Besides the diagnostics that were used to measure the fluctuations, a rough classification, the measured frequency range, determined n and/or m, propagation direction with respect to the laboratory frame, further details and the corresponding references are provided. Following the very detailed studies on AUG and the variety of discussed literature, at least three categories of fluctuations, likely related to different kind of instabilities were identified (c.f. Section 5):

Category 1 appears at medium frequency range (30 kHz to 150 kHz), typical onset after a brief quiet phase with respect to the previous ELM crash (after phase I), multiple bands also named ‘washboard modes’, localized close to the separatrix, ballooned mode structure, n in the region from 3 to 8

Table 1
Summary of observed inter-ELM pedestal fluctuations in several tokamaks.

experiment	diagnostic	Category	Frequency	Mode numbers	propagation relative to laboratory frame	details	reference
AUG	MCs (radial magnetic field fluctuations ($\partial B_r/\partial t$), LFS poloidal array), ECE and RFL	like 2	300 kHz to 500 kHz	n between 5 and 10, m from 10 to 15		poloidal mode number m uncertain because purely determined on LFS	[50]
	MCs ($\partial B_r/\partial t$, LFS poloidal and toroidal array)	like 1 and 3	60 kHz to 100 kHz and 20 kHz	$n \sim 8$ and $n \sim 3$	elec. diamagn.		[51]
	MCs	like 2	150 kHz to 200 kHz	m from 7 to 8	elec. diamagn.	link to type-II ELMy regime	[52]
	ECEI	like 3	20 kHz to 50 kHz	$n \sim 18$, $m \sim 74$	elec. diamagn.		[53]
	MCs ($\partial B_r/\partial t$, HFS and LFS)	2	250 kHz to 450 kHz	n from 10 to 12	elec. diamagn.	onset related to profile evolution, rotation with E × B rotation velocity $\nu_{E\times B}$, visible on HFS	[46]
	MCs ($\partial B_r/\partial t$, LFS toroidal array)	1 and 2	50 kHz to 150 kHz and 200 kHz to 220 kHz	n from 2 to 4 (low frequency) and 8 to 10 (high frequency)	elec. diamagn.	more accurate determination of n in different phases of the ELM cycle, different mode branches (distinct rotation)	[47]
	MCs ($\partial B_r/\partial t$, LFS toroidal array)	2	100 kHz to 350 kHz	n from 9 to 11	elec. diamagn.	hydrogen-I (H), deuterium (D) and helium-4 (^{4}He) plasmas	[54]
	MCs ($\partial B_r/\partial t$, LFS toroidal array)	1 and 2	80 kHz to 120 kHz and 220 kHz to 250 kHz	n from 3 to 6 (low frequency) and 8 to 10 (high frequency)	elec. diamagn.	mode structure of ELM crash reproduced in MHD simulation	[55]
	MC ($\partial B_r/\partial t$, LFS), ECE, ECEI, ithium beam (LIB)	like 2 and 3	200 kHz to 250 kHz and 8 kHz		elec. diamagn.	localization with ECEI and LIB	[56]
	MCs ($\partial B_r/\partial t$, LFS toroidal array)	1, 2 and like 3	80 kHz to 120 kHz, 200 kHz to 250 kHz and 5 kHz to 20 kHz	n from 8 to 10 (high frequency)	elec. diamagn.	pre-ELM as well as ELM crash n depend on edge safety factor (q_{95}) and/or pedestal top n_e	[57]
	MCs ($\partial B_r/\partial t$, LFS toroidal array), ECE, ECEI	2 and 3	200 kHz to 250 kHz and 5 kHz to 15 kHz	n from 13 to 14 (low frequency)	elec. diamagn.	localization at pedestal top with ECEI	[58]
	MC ($\partial B_r/\partial t$, LFS)	1 and 2	40 kHz to 100 kHz and 180 kHz to 300 kHz			link to $\max(-\nabla T_i)$ and E_r recovery	[43]
C-Mod	MC (poloidal magnetic field fluctuations ($\partial B_\theta/\partial t$), LFS), RFL, GPI, phase contrast imaging (PCI)	2	250 kHz to 300 kHz	$n \sim 10$	elec. diamagn.	localized in the steep gradient region, onset correlated with pedestal T_e evolution	[59]
	MC ($\partial B_\theta/\partial t$, LFS), RFL, GPI, PCI	2	280 kHz to 330 kHz	$n \sim 10$	elec. diamagn.	low phase velocity relative to $\nu_{E\times B}$	[60]
COMPASS-D	MC ($\partial B_\theta/\partial t$, LFS)	like 1 except for modulation	80 kHz to 130 kHz	n from 4 to 6	elec. diamagn.		[61]
COMPASS	MC ($\partial B_\theta/\partial t$, LFS)	like 1 except for modulation	50 kHz to 70 kHz			bursty modulated mode amplitude	[62]
DIII-D	BES	like 1	50 kHz to 150 kHz and 200 kHz to 400 kHz		ion diamagn. (low frequency) and elec. diamagn. (high frequency)	broadband, opposite propagation direction, amplitude correlated with electron pressure gradient (∇p_e)	[63]
	MCs ($\partial B_\theta/\partial t$ $\partial B_\theta/\partial t$, LFS), BES, Doppler backscattering (DBS)	like 1	30 kHz to 100 kHz	n from 2 to 4	elec. diamagn.	amplitude correlated with electron temperature gradient (∇T_e)	[48]

(*continued on next page*)

Table 1 (*continued*)

experiment	diagnostic	Category	Frequency	Mode numbers	propagation relative to laboratory frame	details	reference
	MC ($\partial B_\theta/\partial t$ $\partial B_\theta/\partial t$, LFS), BES	1 and 3	70 kHz, 100 kHz and 40 kHz			40 kHz mode located further inwards, frequency bands fulfill matching condition, indication for non-linear coupling at the ELM onset	[64]
EAST	MCs, X-mode microwave reflectometer (RFLX)	like 1 and like 3	100 kHz to 150 kHz and 40 kHz to 60 kHz	n from 1 to 3 (low frequency)	elec. diamagn.	in between type-III ELMs and in between type-I ELMs	[65]
	Langmuir probe (LP) floating potential	like 2	250 kHz to 300 kHz		elec. diamagn.	after L-H transition and in between ELMs	[66]
	RFLX	like 3	40 kHz to 80 kHz		elec. diamagn.	coherent mode	[67]
	MCs (LFS), RFL, LI, ECE	3	25 kHz	$n \sim 14$		coherent mode	[68]
	LP floating potential, MCs ($\partial B_\theta/\partial t$, LFS)	like 1 except for modulation	50 kHz to 100 kHz		elec. diamagn.	ELM post-cursor, modulated amplitude	[69]
	LI, ECE	3	15 kHz to 25 kHz			mode amplitude determines length of the ELM cycle	[70]
HL-2A	MCs (LFS, poloidal and toroidal array), LI, RFL, DBS, ECE	1 and 3	50 kHz to 100 kHz and 50 kHz	$n \sim 7$ and $m \sim 21$ (high frequency)	elec. diamagn.		[71]
JET	MCs ($\partial B_\theta/\partial t$, LFS toroidal array), ECE, RFL	like 1	10 kHz to 100 kHz	n from 1 to 15, m from 3 to 30	elec. diamagn.	'washboard modes', ballooning character	[72]
	MCs (LFS toroidal array)	1	10 kHz to 90 kHz	n from 1 to 8	elec. diamagn.	'washboard modes'	[73]
	MCs (LFS poloidal and toroidal array), ECE and RFL		5 kHz to 25 kHz	n from 1 to 13	ion diamagn.	ELM precursor modes, low n inboard outboard symmetric, higher n show ballooning character	[74]
	MCs (LFS)		20 kHz	$n \sim 10$		wavelet analysis, short lived ELM precursors	[75]
	MC (LFS)	like 2	150 kHz to 300 kHz			bursty modulated amplitude	[76]
KSTAR	MCs	like 3	20 kHz to 50 kHz			wavelet analysis	[77]
	MCs, ECEI	like 3	15 kHz	$n \sim 10$	ion diamagn.		[78]
MAST	MCs, CP-DBS	located like 3				broadband magnetic activity, Doppler shifts up to 1.5MHz, fluctuation power modulated throughout the ELM cycle	[35]
NSTX	BES, correlation RFL				ion diamagn.	broadband fluctuations, large correlation length on pedestal top vs. steep gradient region	[79]
PBX-M	MCs ($\partial B_\theta/\partial t$, LFS and HFS, poloidal array)	like 2	200 kHz to 240 kHz	n from 1 to 4		bursty modulated amplitude, HFS signature stronger than low field side	[80]
	MCs ($\partial B_\theta/\partial t$, LFS and HFS, poloidal array)	like 2	25 kHz to 400 kHz	n from 3 to 8	elec. diamagn.	HFS and LFS signature	[81]

Category 2 appears at high frequencies (larger than 200 kHz), onset connected to T_e pedestal evolution (after phase II), relatively broadband spectrum (width in the region of several tens of kilohertz), localized close to the $\nu_{E\times B}$ minimum, HFS magnetic response, n in the region from 8 to 12.
Category 3 appears at low frequencies (smaller than 30 kHz), localized at the pedestal top close to the $\nu_{E\times B}$ zero crossing, n of roughly 13 to 14. Might be also related to short lived ELM precursor modes.

This is a rather rough and experiment-based classification mainly focusing on similarities that occur for a variety of experiments. The detected frequency range in the lab frame is a rather vague quantity since it depends on the structure of the instability as well as its rotation with respect to the lab frame. However, it's the only quantity that is consistently determined across the variety of work presented in Table 1. Even the determined n and m have to be handled with care, since the extraction of high mode numbers, appearing at high frequencies becomes rather challenging. Typically, MCs have a frequency dependent phase response, which needs to be taken into account, to reconstruct the mode numbers accurately [82]. For the m, the so-called θ^* effect, i.e. the transformation into the straight field line angle (θ^*) coordinate system [83,84], needs to be considered, which requires an exact reconstruction of the plasma equilibrium. Here, 2-D imaging diagnostics such as BES, ECEI or gas puff imaging (GPI) have an advantage. Nevertheless, an exact model is required to interlink the actually measured quantity with the plasma parameters to determine spatial structure sizes or exactly localize the instabilities. In summary, the analyzed mode numbers spread over a range, but are not contradicting. Assuming field aligned instabilities it is expected that the instability structure changes when varying (q). For this reason variations of the mode numbers are possible depending on operational parameters.

It is of importance to point out that there are various similarities of the inter-ELM pedestal fluctuations across different tokamaks. As H-mode itself, it seems that the inter-ELM pedestal instabilities have a similar behavior for the operational parameter ranges in most machines. Further, the instabilities, i.e. fluctuations onsets, are linked to pedestal profile evolution. This correlation points towards an impact on pedestal dynamics e.g. by clamping of maximum gradients. The following section illustrates a bare, conceptual picture of the structure of selected fluctuation categories.

5. Structure of pedestal fluctuations

From the variety of observed mode numbers, the underlying instabilities are expected to have relatively large toroidal and poloidal scales in the region of several tens of centimeter. Further, since the instabilities are observed as fluctuations, they need to rotate with respect to the lab frame. As $\nu_{E\times B}$ is present in the pedestal region this can be a significant contribution to the instabilities' rotation. So far, there was no clear case reported in literature, where a significant phase velocity of the instability could be extracted, appropriately considering and removing the background $\nu_{E\times B}$. This could be also interpreted such that a possible phase velocity of the instability, whose sign would give important information on its generation mechanism, might be small in comparison to the $\nu_{E\times B}$ at the location of the mode.

Fig. 4 illustrates the poloidal mode structures (with exaggerated radial extent) for category 1 (light blue/blue), category 2 (orange/red) and category 3 (magenta/purple) instabilities. These are expected to appear as field aligned structures, since their mode numbers can be determined by tracking them around the torus. While the category 1 and 3 instabilities are not seen on the HFS, which gives evidence for a ballooned mode structure, the instabilities of category 2 exhibit a strong HFS amplitude. This important feature helps to make the different categories distinguishable, besides the different frequency ranges they typically are detected in.

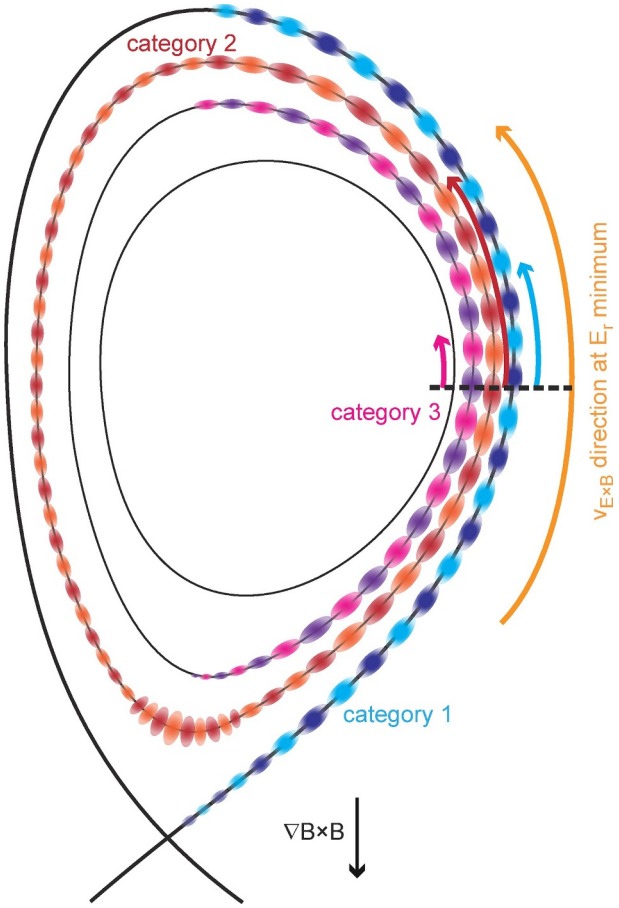

Fig. 4. Illustration of the poloidal mode structure: The medium frequency bands are localized very close to the separatrix and show a ballooning mode structure (blue), while the higher frequency bands are located close to and show a clear HFS high density region signature (red). Further, inwards towards the zero crossing the low frequency fluctuations are localized with dominant LFS amplitude (magenta). All instabilities rotate with $\nu_{E\times B}$ at their location relative to the lab frame.

6. Summary and outlook

This contribution combines experimental observations from a variety of studies at different tokamaks. It is presenting that at least three kinds of distinguishable inter-ELM fluctuations appear in the ELM cycle. Their onset is linked to the evolution of the pedestal gradients and the detected fluctuation frequencies in the lab-frame is dominated by the background rotation of the plasma. The high-level, common features of the inter-ELM fluctuations were identified over a wide range of operational parameters.

To further characterize and localize the instabilities future studies should emphasize the two dimensional aspect of the instabilities and use advanced diagnostics to determine their structure in the poloidal cross section as well as their localization within the pedestal. The impact on the pedestal structure needs to be further clarified. Since the onsets of the fluctuations are correlated to the saturation of pedestal gradients, the instabilities likely cause additional fluxes across the edge. So far it is also unclear how the ELM crash is actually triggered. There could be a connection to the inter-ELM fluctuations. These could either regulate the pedestal at PB stable level before disappearing and letting the pedestal evolve to an unstable structure, i.e. the pedestal width increases, or radial coupling of the distinct, localized instabilities could also trigger the ELM onset [64].

Disclaimer

Acknowledgments

This work was supported by the U.S. Department of Energy under DC-AC02-09Ch11466, DE-SC0015878 and DE-SC0015480.

Supplementary material

Supplementary material associated with this article can be found, in the online version, at 10.1016/j.nme.2019.02.030

References

[1] F. Wagner, et al., Regime of improved confinement and high-beta in neutral-beam-heated divertor discharges of the ASDEX tokamak, Phys. Rev. Lett. 49 (19) (1982) 1408–1412, https://doi.org/10.1103/PhysRevLett.49.1408.
[2] A.E. Hubbard, Physics and scaling of the H-mode pedestal, Plasma Phys. Contr. Fusion 42 (5A) (2000) A15–A35, https://doi.org/10.1088/0741-3335/42/5a/302.
[3] F. Wagner, A quarter-century of H-mode studies, Plasma Phys. Contr. Fusion 49 (12b) (2007) B1–B33, https://doi.org/10.1088/0741-3335/49/12b/S01.
[4] M. Shimada, et al., Progress in the iter physics basis: chapter 1: overview and summary, Nucl. Fusion 47 (6) (2007) S1–S17, https://doi.org/10.1088/0029-5515/47/6/s01.
[5] H. Zohm, Edge localized modes (ELMs), Plasma Phys. Contr. Fusion 38 (2) (1996) 105–128, https://doi.org/10.1088/0741-3335/38/2/001.
[6] A.W. Leonard, Edge-localized-modes in tokamaks, Phys. Plasmas 21 (9) (2014) 090501, https://doi.org/10.1063/1.4894742.
[7] A.W. Leonard, et al., Divertor heat and particle flux due to ELMs in DIII-D and ASDEX-Upgrade, J. Nucl. Mater. 241 (1997) 628–632, https://doi.org/10.1016/S0022-3115(97)80112-2.
[8] A. Loarte, et al., Characteristics of type I ELM energy and particle losses in existing devices and their extrapolation to ITER, Plasma Phys. Contr. Fusion 45 (9) (2003) 1549–1569, https://doi.org/10.1088/0741-3335/45/9/302.
[9] P.T. Lang, et al., ELM control strategies and tools: status and potential for ITER, Nucl. Fusion 53 (4) (2013) 043004, https://doi.org/10.1088/0029-5515/53/4/043004.
[10] A. Loarte, et al., Progress on the application of ELM control schemes to ITER scenarios from the non-active phase to DT operation, Nucl. Fusion 54 (3) (2014), https://doi.org/10.1088/0029-5515/54/3/033007.
[11] H. Meyer, et al., Overview of progress in european medium sized tokamaks towards an integrated plasma-edge/wall solution, Nucl. Fusion 57 (10) (2017) 102014, https://doi.org/10.1088/1741-4326/aa6084.
[12] P.B. Snyder, et al., Edge localized modes and the pedestal: a model based on coupled peeling-ballooning modes, Phys. Plasmas 9 (5) (2002) 2037–2043, https://doi.org/10.1063/1.1449463.
[13] P.B. Snyder, et al., Development and validation of a predictive model for the pedestal height, Phys. Plasmas 16 (5) (2009) 056118, https://doi.org/10.1063/1.3122146.
[14] D. Dickinson, et al., Kinetic instabilities that limit beta in the edge of a tokamak plasma: a picture of an H-mode pedestal, Phys. Rev. Lett. 108 (13) (2012) 135002, https://doi.org/10.1103/PhysRevLett.108.135002.
[15] S. Saarelma, et al., MHD and gyro-kinetic stability of JET pedestals, Nucl. Fusion 53 (12) (2013), https://doi.org/10.1088/0029-5515/53/12/123012.
[16] X.Q. Xu, et al., Gyro-fluid and two-fluid theory and simulations of edge-localized-modes, Phys. Plasmas 20 (5) (2013), https://doi.org/10.1063/1.4801746.
[17] D.R. Hatch, et al., Gyrokinetic study of ASDEX Upgrade inter-ELM pedestal profile evolution, Nucl. Fusion 55 (6) (2015) 063028, https://doi.org/10.1088/0029-5515/55/6/063028.
[18] X.Q. Xu, et al., Toward integrated multi-scale pedestal simulations including edge-localized-mode dynamics, evolution of edge-localized-mode cycles, and continuous fluctuations, Phys. Plasmas 23 (5) (2016) 055901, https://doi.org/10.1063/1.4948283.
[19] T.F. Tang, et al., Quasi-coherent mode simulation during inter-ELM period in HL-2A, Phys. Plasmas 25 (12) (2018), https://doi.org/10.1063/1.5050853.
[20] O. Sauter, et al., Neoclassical conductivity and bootstrap current formulas for general axisymmetric equilibria and arbitrary collisionality regime, Phys. Plasmas 6 (7) (1999) 2834–2839, https://doi.org/10.1063/1.873240.
[21] M.G. Dunne, et al., The role of the density profile in the ASDEX-Upgrade pedestal structure, Plasma Phys. Contr. Fusion 59 (1) (2017) 014017, https://doi.org/10.1088/0741-3335/59/1/014017.
[22] E. Stefanikova, et al., Effect of the relative shift between the electron density and temperature pedestal position on the pedestal stability in JET-ILW and comparison with JET-C, Nucl. Fusion 58 (5) (2018), https://doi.org/10.1088/1741-4326/aab216.
[23] H. Urano, Pedestal structure in H-mode plasmas, Nucl. Fusion 54 (11) (2014) 116001, https://doi.org/10.1088/0029-5515/54/11/116001.
[24] P. Manz, et al., Velocimetry analysis of type-I edge localized mode precursors in ASDEX Upgrade, Plasma Phys. Contr. Fusion 56 (3) (2014) 035010, https://doi.org/10.1088/0741-3335/56/3/035010.
[25] H. Biglari, et al., Influence of sheared poloidal rotation on edge turbulence, Phys. Fluids B-Plasma Phys. 2 (1) (1990) 1–4, https://doi.org/10.1063/1.859529.
[26] E. Viezzer, et al., Evidence for the neoclassical nature of the radial electric field in the edge transport barrier of ASDEX Upgrade, Nucl. Fusion 54 (1) (2014) 012003, https://doi.org/10.1088/0029-5515/54/1/012003.
[27] P.A. Schneider, et al., Analysis of temperature and density pedestal gradients in AUG, DIII-D and JET, Nucl. Fusion 53 (7) (2013) 073039, https://doi.org/10.1088/0029-5515/53/7/073039.
[28] E. Viezzer, et al., Investigation of inter-ELM ion heat transport in the H-mode pedestal of ASDEX Upgrade plasmas, Nucl. Fusion 57 (2) (2017) 022020, https://doi.org/10.1088/0029-5515/57/2/022020.
[29] E. Viezzer, et al., Ion heat transport dynamics during edge localized mode cycles at ASDEX Upgrade, Nucl. Fusion 58 (2) (2018), https://doi.org/10.1088/1741-4326/aaa22f.
[30] A.V. Chankin, et al., SOLPS modelling of ASDEX Upgrade H-mode plasma, Plasma Phys. Contr. Fusion 48 (6) (2006) 839–868, https://doi.org/10.1088/0741-3335/48/6/010.
[31] M.N.A. Beurskens, et al., Pedestal and scrape-off layer dynamics in ELMy H-mode plasmas in JET, Nucl. Fusion 49 (12) (2009) 125006, https://doi.org/10.1088/0029-5515/49/12/125006.
[32] C.F. Maggi, et al., Studies of the pedestal structure and inter-ELM pedestal evolution in JET with the ITER-like wall, Nucl. Fusion 57 (11) (2017) 116012, https://doi.org/10.1088/1741-4326/aa7e8e.
[33] D. Dickinson, et al., Towards the construction of a model to describe the inter-ELM evolution of the pedestal on MAST, Plasma Phys. Contr. Fusion 53 (11) (2011) 115010, https://doi.org/10.1088/0741-3335/53/11/115010.
[34] R. Scannell, et al., Inter-edge localized mode pedestal evolution on MAST and impact of resonant magnetic perturbations, Plasma Phys. Contr. Fusion 55 (3) (2013) 035013, https://doi.org/10.1088/0741-3335/55/3/035013.
[35] J.C. Hillesheim, et al., Intermediate-k density and magnetic field fluctuations during inter-ELM pedestal evolution in MAST, Plasma Phys. Contr. Fusion 58 (1) (2015) 014020, https://doi.org/10.1088/0741-3335/58/1/014020.
[36] R. Behn, et al., Edge profiles of electron temperature and density during ELMy H-mode in ohmically heated TCV plasmas, Plasma Phys. Contr. Fusion 49 (8) (2007) 1289–1308, https://doi.org/10.1088/0741-3335/49/8/013.
[37] R.J. Groebner, et al., Temporal evolution of H-mode pedestal in DIII-D, Nucl. Fusion 49 (4) (2009) 045013, https://doi.org/10.1088/0029-5515/49/4/045013.
[38] A. Burckhart, et al., Inter-ELM behaviour of the electron density and temperature pedestal in ASDEX Upgrade, Plasma Phys. Contr. Fusion 52 (10) (2010) 105010, https://doi.org/10.1088/0741-3335/52/10/105010.
[39] F.M. Laggner, et al., Plasma shaping and its impact on the pedestal of ASDEX Upgrade: Edge stability and inter-ELM dynamics at varied triangularity, Nucl. Fusion 58 (4) (2018), https://doi.org/10.1088/1741-4326/aaaa43.
[40] M.R. Wade, et al., Edge-localized-mode–induced transport of impurity density, energy, and momentum, Phys. Rev. Lett. 94 (22) (2005) 225001, https://doi.org/10.1103/PhysRevLett.94.225001.
[41] M.R. Wade, et al., Edge impurity dynamics during an edge-localized mode cycle on DIII-D, Phys. Plasmas 12 (5) (2005) 056120, https://doi.org/10.1063/1.1891745.
[42] M. Cavedon, et al., Pedestal and E_r profile evolution during an edge localized mode cycle at ASDEX Upgrade, Plasma Phys. Contr. Fusion 59 (10) (2017) 105007, https://doi.org/10.1088/1361-6587/aa7ad0.
[43] M. Cavedon, et al., On the ion and electron temperature recovery after the ELM-crash at ASDEX Upgrade, Nucl. Mater. Energy 18 (2019) 275–280, https://doi.org/10.1016/j.nme.2018.12.034.
[44] M.G. Dunne, et al., Measurement of neoclassically predicted edge current density at ASDEX Upgrade, Nucl. Fusion 52 (12) (2012) 123014, https://doi.org/10.1088/0029-5515/52/12/123014.
[45] L. Horvath, et al., Inter-ELM evolution of the edge current density in JET-ILW type I ELMy H-mode plasmas, Plasma Phys. Contr. Fusion 60 (8) (2018), https://doi.org/10.1088/1361-6587/aac7a9.
[46] F.M. Laggner, et al., High frequency magnetic fluctuations correlated with the inter-ELM pedestal evolution in ASDEX Upgrade, Plasma Phys. Contr. Fusion 58 (6) (2016) 065005, https://doi.org/10.1088/0741-3335/58/6/065005.
[47] F. Mink, et al., Toroidal mode number determination of ELM associated phenomena on ASDEX Upgrade, Plasma Phys. Contr. Fusion 58 (12) (2016) 125013, https://doi.org/10.1088/0741-3335/58/12/125013.
[48] A. Diallo, et al., Correlations between quasi-coherent fluctuations and the pedestal evolution during the inter-edge localized modes phase on DIII-D, Phys. Plasmas 22 (5) (2015) 056111, https://doi.org/10.1063/1.4921148.

[49] F.M. Laggner, et al., Divertor, scrape-off layer and pedestal particle dynamics in the ELM cycle on ASDEX Upgrade, Plasma Phys. Contr. Fusion 60 (2) (2018), https://doi.org/10.1088/1361-6587/aa90bf.
[50] T. Bolzonella, et al., High frequency MHD activity related to type I ELMs in ASDEX Upgrade, Plasma Phys. Contr. Fusion 46 (5A) (2004) A143–A149, https://doi.org/10.1088/0741-3335/46/5a/015.
[51] J. Neuhauser, et al., Structure and dynamics of spontaneous and induced ELMs on ASDEX Upgrade, Nucl. Fusion 48 (4) (2008) 045005, https://doi.org/10.1088/0029-5515/48/4/045005.
[52] C.P.P. von Thun, et al., Identifying the MHD signature and power deposition characteristics associated with type-II ELMs in ASDEX Upgrade, Plasma Phys. Contr. Fusion 50 (6) (2008) 065018, https://doi.org/10.1088/0741-3335/50/6/065018.
[53] J.E. Boom, et al., 2D ECE measurements of type-I edge localized modes at ASDEX Upgrade, Nucl. Fusion 51 (10) (2011) 103039, https://doi.org/10.1088/0029-5515/51/10/103039.
[54] F.M. Laggner, et al., Pedestal structure and inter-ELM evolution for different main ion species in ASDEX Upgrade, Phys. Plasmas 24 (5) (2017) 056105, https://doi.org/10.1063/1.4977461.
[55] A.F. Mink, et al., Nonlinear coupling induced toroidal structure of edge localized modes, Nucl. Fusion 58 (2) (2018), https://doi.org/10.1088/1741-4326/aa98f7.
[56] B. Vanovac, et al., Effects of density gradients and fluctuations at the plasma edge on ECEI measurements at ASDEX Upgrade, Plasma Phys. Contr. Fusion 60 (4) (2018), https://doi.org/10.1088/1361-6587/aaa7ac.
[57] A.F. Mink, et al., Scaling of the toroidal structure and nonlinear dynamics of ELMs on ASDEX Upgrade, Plasma Phys. Contr. Fusion 60 (12) (2018), https://doi.org/10.1088/1361-6587/aae33a.
[58] B. Vanovac, et al., Characterization of low-frequency inter-ELM modes of H-mode discharges at ASDEX Upgrade, Nucl. Fusion 58 (11) (2018), https://doi.org/10.1088/1741-4326/aada20.
[59] A. Diallo, et al., Observation of edge instability limiting the pedestal growth in tokamak plasmas, Phys. Rev. Lett. 112 (11) (2014) 115001, https://doi.org/10.1103/PhysRevLett.112.115001.
[60] A. Diallo, et al., Quasi-coherent fluctuations limiting the pedestal growth on Alcator C-mod: experiment and modelling, Nucl. Fusion 55 (5) (2015) 053003, https://doi.org/10.1088/0029-5515/55/5/053003.
[61] A.L. Colton, et al., Elm studies on the COMPASS-D tokamak, Plasma Phys. Contr. Fusion 38 (8) (1996) 1359–1365, https://doi.org/10.1088/0741-3335/38/8/037.
[62] M. Spolaore, et al., Electromagnetic elm and inter-ELM filaments detected in the COMPASS scrape-off layer, Nuclear Mater. Energy (2016), https://doi.org/10.1016/j.nme.2016.12.014.
[63] Z. Yan, et al., Pedestal density fluctuation dynamics during the inter-ELM cycle in DIII-D, Phys. Plasmas 18 (5) (2011) 056117, https://doi.org/10.1063/1.3590936.
[64] A. Diallo, et al., Direct observation of nonlinear coupling between pedestal modes leading to the onset of edge localized modes, Phys. Rev. Lett. 121 (23) (2018) 235001, https://doi.org/10.1103/PhysRevLett.121.235001.
[65] X. Gao, et al., Observation of pedestal plasma turbulence on EAST tokamak, Plasma Sci. Technol 15 (8) (2013) 732–737, https://doi.org/10.1088/1009-0630/15/8/03.
[66] H.Q. Wang, et al., Observation of a quasi-coherent high-frequency electromagnetic mode at the pedestal region in EAST RF-dominant H-modes, Nucl. Fusion 54 (4) (2014), https://doi.org/10.1088/0029-5515/54/4/043014.
[67] X. Gao, et al., Experimental study of pedestal turbulence on EAST tokamak, Nucl. Fusion 55 (8) (2015) 083015, https://doi.org/10.1088/0029-5515/55/8/083015.
[68] T. Zhang, et al., Outward particle transport by coherent mode in the H-mode pedestal in the experimental advanced superconducting tokamak (EAST), Plasma Phys. Contr. Fusion 59 (6) (2017) 065012, https://doi.org/10.1088/1361-6587/aa69e8.
[69] N. Zhao, et al., The observation of small ELM post-cursor mode in EAST, Plasma Sci. Technol 20 (2) (2018) 024007, https://doi.org/10.1088/2058-6272/aa9477.
[70] F.B. Zhong, et al., Effect of pedestal fluctuation on ELM frequency in the EAST tokamak, Nucl. Fusion 58 (5) (2018), https://doi.org/10.1088/1741-4326/aab30a.
[71] W.L. Zhong, et al., Excitation of edge plasma instabilities and their role in pedestal saturation in the HL-2A tokamak, Plasma Phys. Contr. Fusion 58 (6) (2016) 065001, https://doi.org/10.1088/0741-3335/58/6/065001.
[72] P. Smeulders, et al., Characteristics of a new class of transport-related MHD modes in JET H-mode plasmas, Plasma Phys. Contr. Fusion 41 (10) (1999) 1303–1320, https://doi.org/10.1088/0741-3335/41/10/307.
[73] C.P. Perez, et al., Washboard modes as ELM-related events in JET, Plasma Phys. Contr. Fusion 46 (1) (2004) 61–87, https://doi.org/10.1088/0741-3335/46/1/005.
[74] C.P. Perez, et al., Type-I ELM precursor modes in JET, Nucl. Fusion 44 (5) (2004) 609–623, https://doi.org/10.1088/0029-5515/44/5/005.
[75] F.M. Poli, et al., Study of the spectral properties of ELM precursors by means of wavelets, Plasma Phys. Contr. Fusion 50 (9) (2008), https://doi.org/10.1088/0741-3335/50/9/095009.
[76] C. Bowman, et al., Pedestal evolution physics in low triangularity JET tokamak discharges with ITER-like wall, Nucl. Fusion 58 (1) (2018), https://doi.org/10.1088/1741-4326/aa90bc.
[77] J.W. Ahn, et al., Confinement and ELM characteristics of H-mode plasmas in KSTAR, Nucl. Fusion 52 (11) (2012) 114001, https://doi.org/10.1088/0029-5515/52/11/114001.
[78] M. Kim, et al., Multimode excitation during the inter-ELM-crash periods in KSTAR H-mode plasma, Nucl. Fusion 55 (7) (2015) 073001, https://doi.org/10.1088/0029-5515/55/7/073001.
[79] A. Diallo, et al., Observation of ion scale fluctuations in the pedestal region during the edge-localized-mode cycle on the national spherical torus experiment, Phys Plasmas 20 (1) (2013) 012505, https://doi.org/10.1063/1.4773402.
[80] S.M. Kaye, et al., Characteristics of high-frequency ELM precursors and edge stability in the PBX-M tokamak, Nucl. Fusion 30 (12) (1990) 2621–2627, https://doi.org/10.1088/0029-5515/30/12/016.
[81] S.M. Kaye, et al., ELM-related fluctuations in PBX-M H-modes, Plasma Phys. Contr. Fusion 36 (7) (1994) A135–A140, https://doi.org/10.1088/0741-3335/36/7a/017.
[82] L. Horvath, et al., Reducing systematic errors in time-frequency resolved mode number analysis, Plasma Phys. Contr. Fusion 57 (12) (2015) 125005, https://doi.org/10.1088/0741-3335/57/12/125005.
[83] O. Klüber, et al., MHD mode structure and propagation in the ASDEX tokamak, Nucl. Fusion 31 (5) (1991) 907–926, https://doi.org/10.1088/0029-5515/31/5/008.
[84] M. Schittenhelm, et al., Analysis of coupled MHD modes with Mirnov probes in ASDEX Upgrade, Nucl. Fusion 37 (9) (1997) 1255–1270, https://doi.org/10.1088/0029-5515/37/9/I06.